PCCP

PAPER

View Article Online
View Journal | View Issue

Cite this: *Phys. Chem. Chem. Phys.*, 2017, **19**, 7910

Controlling the termination and photochemical reactivity of the $SrTiO_3$(110) surface†

Yisi Zhu, Paul A. Salvador and Gregory S. Rohrer*

$SrTiO_3$(110) orientated crystals have been heated to temperatures between 1000 °C and 1200 °C in air, alone or in the presence of powder reservoirs of TiO_2 or $Sr_3Ti_2O_7$. In these conditions, the surface is terminated by two types of atomically flat terraces. One has a relatively higher surface potential and promotes the photochemical reduction of silver (it is photocathodic) and the other has a relatively lower surface potential and promotes the photochemical oxidation of lead (it is photoanodic). Measurements of the step heights between the terraces indicate that the surfaces with different properties have different terminations. By adjusting the time and temperature of the anneal, and in some cases including reservoirs of TiO_2 or $Sr_3Ti_2O_7$, it is possible to change the surface area fraction from 98% photocathodic to 100% photoanodic. The surface is more photocathodic when the annealing temperature is lower, the duration shorter, and if $Sr_3Ti_2O_7$ is present. The surface is more photoanodic if the temperature is higher, the annealing duration longer, and if TiO_2 is present. The results make it possible to control the surface potential and the ratio of photocathodic to photoanodic area on the $SrTiO_3$(110) surface.

Received 17th December 2016,
Accepted 23rd February 2017

DOI: 10.1039/c6cp08608j

rsc.li/pccp

Introduction

Photocatalyzed water splitting using solar radiation is a promising method for the large-scale production of hydrogen, a clean, high energy density fuel. To split water, photogenerated electrons and holes must migrate to the catalyst surface where they can reduce and oxidize water to produce hydrogen and oxygen, respectively.[1–4] For colloidal catalysts, the reduction and oxidation reactions must both happen on the surface of one particle and with no externally applied potential. These constraints lead to unacceptably high rates of photogenerated charge carrier recombination and the back-reaction of intermediate chemical species. As a result, the sunlight-to-hydrogen conversion efficiencies of colloidal photocatalysts are too low to support commercial hydrogen production.[5,6] It is possible, however, to control internal fields near the surface of photocatalyst powders that influence charge carrier transport, increasing the efficiency by separating photogenerated carriers (reducing recombination) and separating the location of the half reactions (reducing back-reaction).[7,8] The simplest approach is to add a sparse amount of a co-catalyst to generate a phase boundary.[9] Internal fields can also arise in single compound photocatalysts from: ferroelectric polarization,[10–12] flexoelectric phenomena,[13,14] polymorph boundaries,[15,16] differently charged facets/orientations,[17,18] as well as differently terminated surfaces of the same orientation.[19–21] In this paper, we continue to explore how surface termination of an individual crystal orientation can be manipulated to influence the overall photochemical reactivity.

There are a number of materials that have been shown to have, on the same surface orientation, some areas that promote reduction reactions (we will refer to such surfaces as photocathodic) and other areas that promote oxidation reactions (we will refer to such surfaces as photoanodic).[11,14,19] To optimize the overall efficiency of photocatalysis, it is important to control the ratios of the photoanodic to photocathodic areas, such that the two half reactions occur at the same overall rate. When controlling the surface properties with co-catalysts, this balance might be achieved empirically. For photocatalysts with internal fields that naturally have a combination of photoanodic and photocathodic areas, achieving the proper ratio is less straightforward, although some control has been achieved by controlling the shapes of faceted particles.[22,23] We recently showed that, on bulk $SrTiO_3$(111) crystals, the relative area of photoanodic (photocathodic) reactivity could be controlled from 45 to 86% (55 to 14%) using a thermo-chemical annealing procedure that takes advantage of the polar terminations on the $SrTiO_3$(111) surface.[21] Here, we extend this thermo-chemical annealing method, apply it to the $SrTiO_3$(110) surface, explore a wider range of annealing conditions, and demonstrate that the photocathodic-to-photoanodic surface area ratio can be tuned to nearly any value.

Strontium titanate ($SrTiO_3$) is a well-known cubic perovskite (lattice constant $a = 3.905$ Å[24]) photocatalyst that can split water

---

Department of Materials Science and Engineering, Carnegie Mellon University, Pittsburgh, PA 15213, USA. E-mail: gr20@andrew.cmu.edu

† Electronic supplementary information (ESI) available: Additional AFM images support the conclusions. See DOI: 10.1039/c6cp08608j

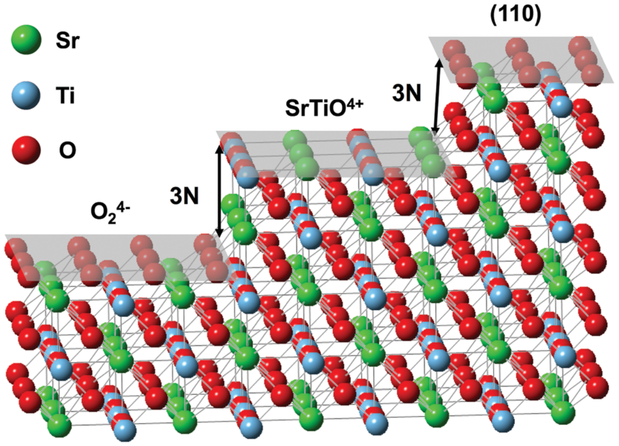

Fig. 1 Schematic of $SrTiO_3$ viewed along [001] direction. The (110) surfaces are highlighted by the transparent grey planes. Along the [110] direction, $SrTiO_3$ is comprised of alternating $(SrTiO)^{4+}$ and $(2O)^{4-}$ layers separated by N = 1.38 Å.

under UV-light irradiation[25] (band gap = 3.25 eV[26]). As illustrated in Fig. 1, the bulk-terminated $SrTiO_3(110)$ surface is polar, which means that the atomically flat surface terraces have a net charge. The unreconstructed bulk-terminated polar $SrTiO_3(110)$ surface has a composition and charge of either $(SrTiO)^{4+}$ or $(2O)^{4-}$. It has already been shown that this surface has distinct photocathodic and photoanodic terraces[19] that are separated by the distance between dissimilar chemical terminations. As indicated in Fig. 1, the spacing between these two layers is $N = \sqrt{2}a/4 = 1.38$ Å, and terraces of the same (different) chemical component are separated by step heights that are even multiples of N (odd multiples of N). Similar observations were made on $SrTiO_3(111)$ surfaces,[19,21] and recently it was shown that the surface potential, measured using Kelvin Probe Force Microscopy (KFM), also correlated with the step heights and chemical reactivity of the (111) surface.[21]

The electric potential of a semiconductor surface is determined by the work function and local surface charge. As such, it is an indicator of the near surface internal fields, which affect the relative reactivity of a surface. For an n-type semiconductor (such as $SrTiO_3$), a reduced work function or a positive surface charge results in a greater surface potential. The energy bands are bent downward (from the flat band condition) at such a surface, which results in electrons being attracted to the surface. On the other hand, a larger work function or a negative surface charge leads to a lower surface potential, upward band bending at the surface, and holes being attracted to that surface. Even if the work functions of the different terminations of $SrTiO_3$ are similar, the polar surfaces should still exhibit different surface potentials, and this will affect the reactivity. Observations on the polar $SrTiO_3(111)$ surface are consistent with this idea.[21]

Because photocatalyst samples are exposed to air and aqueous solutions, the active $SrTiO_3(111)$ and (110) polar surfaces are likely to differ from the ideal bulk termination, owing to reconstructions[27–32] and adsorbate layers.[33,34] As such, the amount of surface charge and the extent of the associated space charge region are difficult to quantify, but a qualitative correlation between the relative surface potential and relative reactivity has been established on different $SrTiO_3(111)$ terraces[21] and on different orientations of Fe_2O_3 surfaces.[18] In this work, we demonstrate a similar correlation on different $SrTiO_3(110)$ polar terraces.

Most prior work on controlling the surface chemistry of bulk $SrTiO_3$ single crystals was motivated either by a desire to have completely uniform surfaces that promote high-quality heteroepitaxial crystal growth with defect-free interfaces,[35,36] or to characterize the types of reconstructions that exist for this archetypical perovskite.[37] Thin film surface engineering investigations have largely used soft-chemical, low temperature etching methods (such as with a buffered hydrogen fluoride solution[35]) combined with intermediate-temperature anneals (<1000 °C), while surface structure investigations often focus on intermediate-temperature annealing in different vacuum conditions. On $SrTiO_3(110)$, for example, a uniform oxygen termination was prepared by thermal annealing in ultra-high vacuum,[37] while a uniform $(SrTiO)^{4+}$ termination was prepared by Ar^+ ion sputtering.[32] We recently demonstrated that high-temperature (>1000 °C) anneals in air, with or without Sr–Ti–O containing powder reservoirs, can be used to modify the relative surface termination of the $SrTiO_3(111)$ surface. The three main points of the current paper are to show that the relative surface termination of $SrTiO_3(110)$ can be controlled using thermo-chemical anneals, to show that polar terraces on $SrTiO_3(110)$ have different surface potentials, and to show that the relative reactivity on different polar terraces correlates with the surface potential. This makes it possible to tune the ratio of photoanodic to photocathodic reactive areas.

Experimental

A chemical-mechanical polished $SrTiO_3(110)$ single crystal (MTI Corporation, Richmond, CA, 1 cm × 1 cm, (110) ± 0.5°, roughness <5 Å) was cut into 16 smaller pieces (2.5 mm × 2.5 mm). Each sample was ultrasonicated in a methanol bath for 10 min, placed in a covered rectangular alumina combustion boat, heated in a muffle furnace (to 1000 °C, 1100 °C or 1200 °C) at a rate of 10 °C min^{-1}, annealed for a time between 0 and 24 h, and then cooled at 10 °C min^{-1}. After annealing, atomically flat terraces were observed by atomic force microscopy (AFM, Solver-Next, NT-MDT, Russia). Selected samples were annealed with reservoirs of TiO_2 or $Sr_3Ti_2O_7$ powder. In these experiments, the $SrTiO_3(110)$ crystal was put at the center of the combustion boat and the powder reservoirs were placed around, but not in contact with, the crystal. The combustion boat was then covered and heated to the designated temperature using the same heating and cooling rate specified above. For the experiments with powder reservoirs, 2 g of TiO_2 or either 0.02 or 0.1 g of $Sr_3Ti_2O_7$ was used. It should be noted that when larger masses (*e.g.*, 2 g) of $Sr_3Ti_2O_7$ were used for the reservoir, Sr-rich particulates were found decorated over the $SrTiO_3(110)$ surface. No particulate surface phases were observed for the masses used, which were all greater than the mass of the $SrTiO_3$ crystal (≈0.015 g).

The photo-reduction of Ag^+ and the photo-oxidation of Pb^{2+} leave insoluble products on the surface at the site of the reaction and were therefore used to mark the locations of the photo-reduction and photo-oxidation reactions.[11,17,19,38,39] Both experiments were carried out in the same way. The sample was placed on a glass slide and surrounded by a viton O-ring (diameter ∼ 0.5 cm). A 0.115 M $AgNO_3$ or $Pb(CH_3COO)_2$ solution was poured into the O-ring and a quartz slip was placed on top, sealing the solution in the O-ring by capillarity and without an air bubble. A fiber optic waveguide attached to a 300 W mercury lamp (Newport, Irvine, CA) was placed with its lens facing downward and in contact with the quartz slip. Typically, the sample was exposed to the light for 4 s, for silver reduction, or 90 s, for lead oxidation. The need for longer exposure times for lead oxidation is thought to be related to the complexity of the oxidation reaction, which involves lead, oxygen, and multiple photo-generated carriers. The reaction rate is also affected by the solution pH (which was ≈4.86 in this work).[40,41] For situations where relative areas of photoanodic or photocathodic terraces neared 100%, the reaction times had to be increased (to 30 s for silver reduction and 150 s for lead oxidation) to generate similar amounts of reaction product on the terraces. This is probably because the rate became limited by the counter reaction that had to occur on a small minority of the surface area. After illumination, the $SrTiO_3(110)$ sample was rinsed with de-ionized water and dried using a stream of nitrogen gas. The products from these two marker reactions can be removed by ultra-sonication in acetone and methanol baths, for 10 min each, and then wiping the surface with a cotton swab.

AFM imaging in tapping mode was used to measure the topography of the annealed $SrTiO_3(110)$ surface before and after reaction (at the same location) to determine the distribution of products created by the photochemical reaction. High-precision AFM images were used to measure the step height between neighboring terraces. As mentioned before, the $SrTiO_3(110)$ terraces are separated by integer multiples of 1.38 Å. The high-precision AFM has a noise level of ≈0.3 Å, making it possible measure the difference between even-*N* and odd-*N* step heights. All topographic images were made with an alumina coated silicon probe with a tip radius of <10 nm (Tap 300AL-G, Budget-Sensors, Bulgaria). The local surface potential of each terrace was measured by KFM using a silicon AFM probe with a PtCr (190E-G, BudgetSensors, Bulgaria) conductive coating. KFM images of the relevant areas of the clean surface were collected before the photochemical reactions. All of the scanning probe microscopy data were processed and analyzed using the Gwyddion software package.[42]

Results

The topography of the clean $SrTiO_3(110)$ surface after annealing for 6 h in air at 1200 °C is shown in Fig. 2a. After annealing, the surface is made up of a terrace and step structure; the roughness on individual terraces is <0.015 nm, so we refer to them as atomically flat. The dominant feature on this surface is the terrace and step structure that is diagonal to the field of view. On these terraces, there are also islands, higher than the principal terraces, that appear as white contrast; a blue line has been added to Fig. 2a that crosses three of these islands. The height trace over these islands (see Fig. 2e) shows that they range in height from 0.3 to 0.7 nm. The surface potential image of the same area is shown in Fig. 2b. Comparing it to Fig. 2a, it is clear that, at the positions of the islands, the potential is higher than the surrounding areas. The potential profile over the islands (see Fig. 2e) shows that the potential at the positions of the islands is 10 to 20 mV greater than the surrounding area.

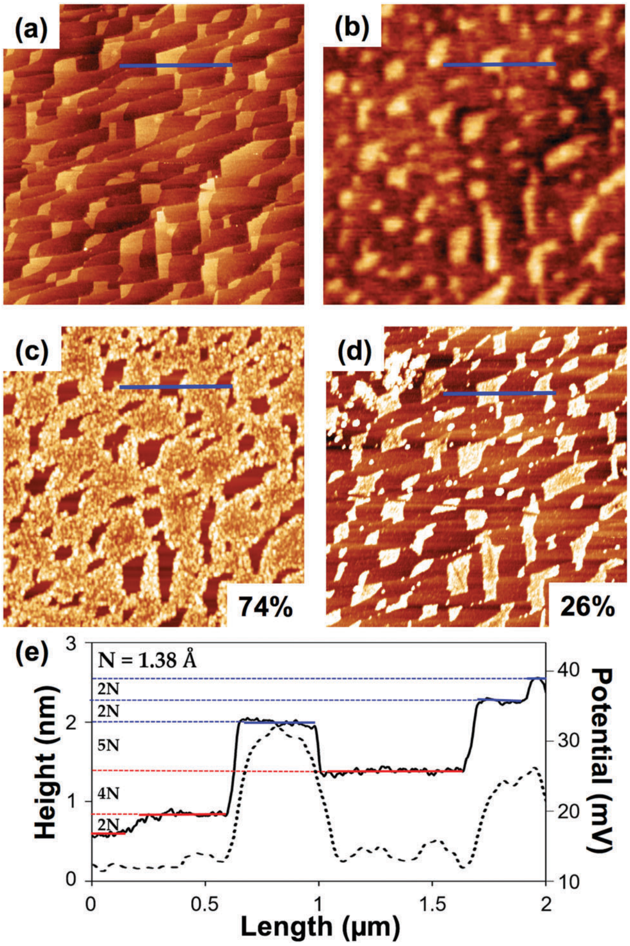

Fig. 2 (a) Topographic AFM image, (b) surface potential image, (c) topographic image after lead photo-oxidation, and (d) topographic image after silver photo-reduction. (a–d) Are the same area of the surface and have a 5 μm × 5 μm field of view. The blue lines mark the same location in each image and are 2 μm in length. The color range from dark-to-light is: (a) 0–2 nm, (b) 0 to 40 mV, (c) 0–6 nm, and (d) 0–4 nm. In (c) and (d), the fractional coverage of photoanodic and photocathodic terraces, respectively, are given in the lower right corner. In (e), the black solid line is the height cross-section at the position of the blue line in (a) and the dashed line is the potential profile at the same position. Red lines mark the photoanodic terraces and blue lines mark the photocathodic terraces.

After the sample was illuminated by a mercury lamp in lead acetate (silver nitrate) solution, new topographic features appeared on the surface corresponding to lead- (silver-) containing deposits, as shown in Fig. 2c (Fig. 2d). Note that Fig. 2a–d show the same area of the surface. Based on the spatial distribution of the reaction products, a majority of the surface promotes oxidation (is photoanodic) and the remainder of the surface promotes reduction (is photocathodic). Because each half-reaction is limited to a different subset of the complete surface, we refer to this as complementary reactivity. Also, when the distribution of reaction products is compared to the surface potential results, we find that the island terraces that have the highest surface potential promote the photo-reduction of silver and the remaining lower potential terraces promote the photo-oxidation of lead. Based on the areal coverage of reaction products in these images, 74% of the surface is photoanodic (oxidizes lead) and 26% is photocathodic (reduces silver).

A high-precision AFM height profile (and surface potential profile) recorded at the position of the blue line on Fig. 2a (Fig. 2b) is plotted as a solid (dashed) line in Fig. 2e. The height profile indicates the line crosses six atomically flat terraces. The average heights of these terraces are 5.59, 8.19, 20.30, 13.75, 22.79, and 25.47 Å, and the variations of height within any given terrace are <0.15 Å. In terms of the intrinsic spacing between parallel (110) layers, $N = 1.38$ Å, the changes in height between the neighboring terraces are $\approx 2N$, $9N$, $-5N$, $7N$, and $2N$. The average potential values are these same terraces are 11, 12, 28, 13, 23, and 25 mV, and the variations of potential within any given terrace are ±10%. Recalling that odd-N height differences between terraces correspond to chemical termination differences, we can see that when two terraces are separated by an even-N step, the potential does not change by more than 5 mV and when two terraces are separated by an odd-N step, the potential changes by more than 10 mV. These results indicate that the surface potential correlates with the surface termination. There is also a correlation with reactivity. From left to right, the first, second, and fourth terraces are reactive for the photo-oxidation of lead (see Fig. 2c and the dashed red lines in Fig. 2e), while the third, fifth and sixth terraces are reactive for the photo-reduction of silver (see Fig. 2d and the dashed blue lines in Fig. 2e). The photoanodic terraces have potentials that are similar to one another and are separated from each other by even-N heights, suggesting that they all have the same chemical termination. The photocathodic terraces also have potentials that are similar to one another and are also separated from each other by even-N heights, suggesting that they also all have the same chemical termination. Photoanodic and photocathodic terraces have different potentials and are separated by odd-N heights, indicating that there is a change in the chemical termination. This correlation between the termination, potential, and reactivity explains the complementary nature of the photochemical reactivity of the $SrTiO_3$(110) surfaces.

To control the chemical termination and surface reactivity, $SrTiO_3$(110) crystals were annealed for different lengths of time at 1200 °C in air. The surfaces of samples annealed for 0, 3, 12, and 24 h are shown in Fig. 3(a)–(d), respectively, after the photo-oxidation of lead. As in Fig. 2c, the regions of bright contrast in Fig. 3 correspond to Pb-containing deposits. (Images of the same areas after the photo-reduction of silver and before any reaction are shown in Fig. S1 and S2 (ESI†), respectively.) These results show a clear trend: as the annealing time at 1200 °C increases, the photoanodic area fraction (area fraction covered with bright contrast) increases. The photoanodic area fractions increase from 45 to 100% as the annealing time is increased from 0 to 24 h. As was the case in Fig. 2, the reactive areas were complementary (see Fig. S1, ESI†) and the reactivity is correlated to the relative coverage of the two types of terraces in the topographic images (see Fig. S2, ESI†).

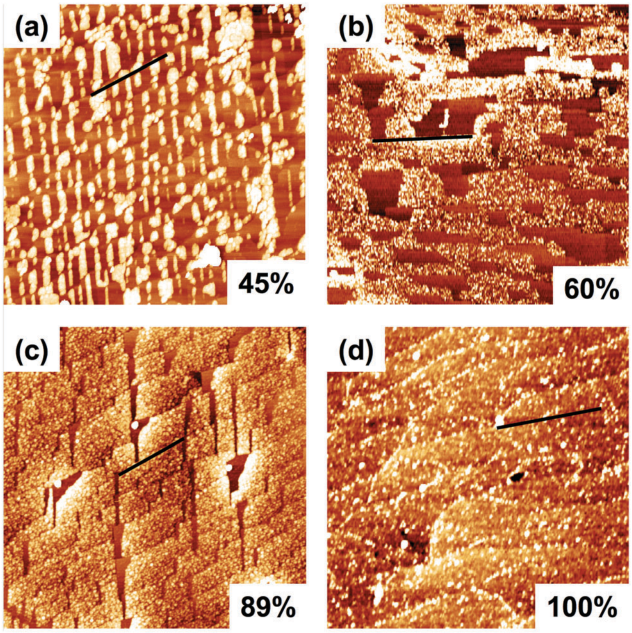

Fig. 3 Topographic AFM images of samples annealed at 1200 °C for (a) 0 h, (b) 3 h, (c) 12 h, and (d) 24 h after the photochemical oxidation of lead. All images are 5 μm × 5 μm and the dark-to-light vertical contrast is 0–6 nm. The fractional coverage of photoanodic terraces is given in the lower right corner. The black lines mark the same locations that are marked in Fig. S1 and S2 (ESI†). Note that these images are from four separate samples, prepared differently, and subjected to identical photooxidation reactions.

To explore the influence of annealing temperature on the surface reactivity, samples were annealed at 1100 and 1000 °C, for both 0 and 6 h. Fig. 4a and b (Fig. 4c and d) show topographic images of these samples after the photo-oxidation of lead for samples heated to 1100 °C (1000 °C) for 0 h and 6 h, respectively. The trend at both temperatures is similar to what was observed at 1200 °C: the fractional coverage of photoanodic terraces increases with annealing time, from 38 to 68% (15 to 32%) for 0 h and 6 h anneals at 1100 °C (1000 °C). By comparing the samples annealed at different temperatures for the same amount of time, the fractional coverage of photoanodic terraces is observed to increase with the annealing temperature. The photoanodic area fractions of samples annealed for 0 h at 1000, 1100, and 1200 °C were 15% (Fig. 4c), 38% (Fig. 4a), and 45% (Fig. 3a), respectively. The photoanodic area fractions of samples annealed for 6 h at 1000, 1100, and 1200 °C were 32% (Fig. 4d), 68% (Fig. 4b), and 74% (Fig. 2c), respectively. Thus, both increased annealing time and increased annealing temperature increase the photoanodic reactivity. However, a completely photocathodic surface was not achieved in these conditions: the highest relative photocathodic

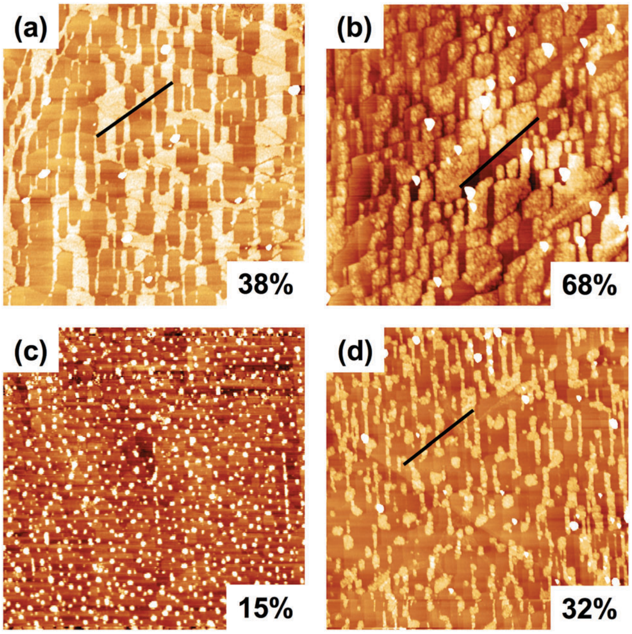

Fig. 4 Topographic AFM images after lead photo-oxidation for samples annealed at 1100 °C for (a) 0 h (b) 6 h and samples annealed at 1000 °C for (c) 0 h (d) 6 h. Lateral image dimensions are: (a), (b), and (d) 5 μm × 5 μm, and (c) 3 μm × 3 μm. The dark-to-light vertical scales are (a), (b), and (d) 0–6 nm, and (c) 0–3 nm. The fractional coverage of photoanodic terraces is given in the lower right corner. The black lines mark the same location that is marked in Fig. S3 and S4 (ESI†).

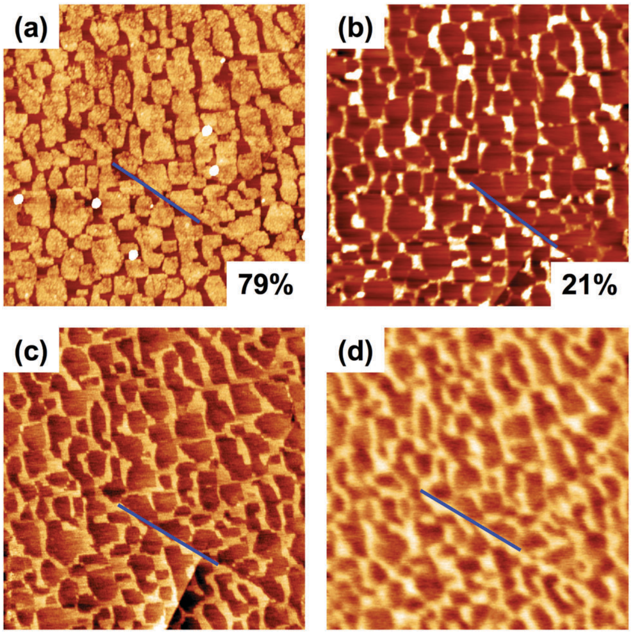

Fig. 5 (a) Topographic AFM image after lead photo-oxidation, (b) topographic image after silver photo-reduction, (c) topographic image of the clean surface, and (d) surface potential image. All images are 5 μm × 5 μm and show the same area on a sample annealed with 2 g TiO_2 powder at 1000 °C for 6 h. The blue lines mark the same locations. The vertical scale from dark-to-light is: (a) 0 to 6 nm, (b) 0 to 4 nm, (c) 0 to 2 nm, and (d) 0 to 40 mV. The fractional coverage of photoanodic and photocathodic terraces in (a) and (b), respectively, are given in the lower right corners.

activity was 85%. The area fractions of the photocathodic surfaces remain complementary in all cases (see Fig. S3, ESI†) and the area fraction of each reactivity is correlated with the relative coverage of the two types of terraces in the topographic data (see Fig. S4, ESI†).

In addition to temperature and time, the annealing environment, controlled by the composition of the powder reservoir placed adjacent to the crystal, can alter the relative area fraction of reactivity.[21] For $SrTiO_3(111)$ crystals, heating in the presence of excess TiO_2 increased the surface Ti/Sr ratio and the photoanodic area fraction.[21] Hypothesizing that the $SrTiO_3(110)$ surface composition might be changed in the same way, we annealed several crystals in TiO_2-rich and SrO-rich environments at different temperatures and for different times. First, a sample was annealed at 1000 °C for 6 h while surrounded by 2 g of TiO_2 powder. Images from the sample annealed with TiO_2 powder are shown in Fig. 5. A topographic image recorded after the photo-oxidation (photo-reduction) of lead (silver) is shown in Fig. 5a (Fig. 5b). The surface still exhibits complementary reactivity with the photoanodic (photocathodic) area fraction being 79% (21%). Comparing the sample annealed with (Fig. 5) and without TiO_2 powder (Fig. 4d, which was only 32% photanodic) demonstrates that the addition of TiO_2 more than doubles the fractional coverage of the photoanodic surface, similar to what was observed for $SrTiO_3(111)$.

The topographic and surface potential images of the same location before the reaction are shown in Fig. 5c and d. In the topography data, there are raised islands at the edges of terraces, similar to the sample that was heated without the TiO_2 reservoir (see Fig. 2a). In this case, the islands decorate the edges of the principal terraces and dominate the contrast. The locations of these islands are coincident with the areas of higher surface potential (Fig. 5d) that are photocathodic (Fig. 5b); the complementary areas are photoanodic (see Fig. 5a). The results in Fig. 5 are consistent with those from samples annealed without a powder reservoir, indicating that annealing in the presence of TiO_2 makes the sample more photoanodic, without altering the potential differences between the terraces or the complementary reactivity.

Next, a sample was annealed at 1100 °C for 6 h while surrounded by 0.02 g of $Sr_3Ti_2O_7$ powder, to test the effect of heating in Sr-rich conditions. Images of the sample annealed with $Sr_3Ti_2O_7$ (SrO-excess) powder are shown in Fig. 6. A topographic image recorded after the photo-oxidation (photo-reduction) of lead (silver) is shown in Fig. 6a (Fig. 6b). The photoanodic (photocathodic) area fractions were 44% (56%), again supporting complementarity. Comparing the samples heated with (Fig. 6) and without $Sr_3Ti_2O_7$ powder (Fig. 4b) demonstrates that the addition of a small amount (0.02 g) of $Sr_3Ti_2O_7$ powder decreases the fractional coverage of photoanodic surface, changing it from 68% to 44% of the total area.

In the topography data, island terraces are again visible on the larger flat terraces. As observed for other samples, there is a clear correlation between the island terraces and the contrast in the other images in Fig. 6. Specifically, the higher (lower)

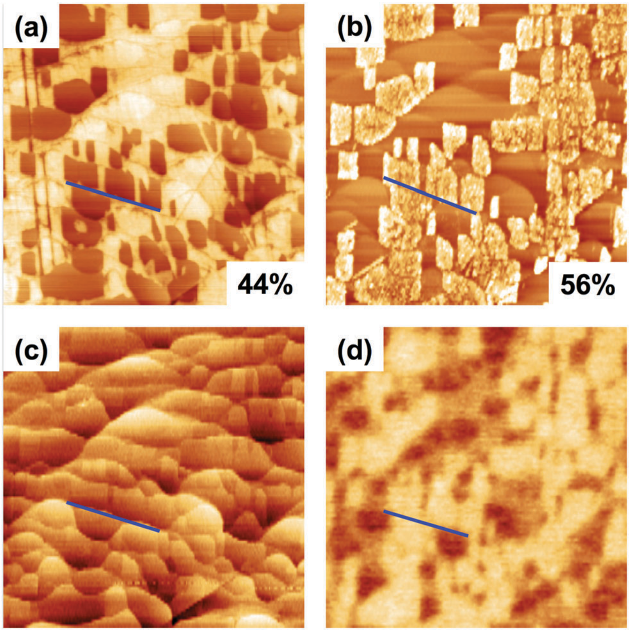

Fig. 6 (a) Topographic AFM image after lead photo-oxidation, (b) topographic image after silver photo-reduction recorded, (c) topographic image of the clean surface, and (d) surface potential image of the same area of the sample annealed at 1100 °C for 6 h with 0.02 $Sr_3Ti_2O_7$. All images are 5 μm × 5 μm. The blue lines mark the same position on each image. The vertical scale from dark-to-light is: (a) 0–6 nm, (b) 0 to 4 nm, (c) 0–4 nm, and (d) 0–40 mV. The fractional coverage of photoanodic and photocathodic terraces in (a) and (b), respectively, are given in the lower right corners.

surface potential areas (Fig. 6d) are correlated to the set of topographically higher (lower) terraces (Fig. 6c) and regions that are photocathodic in Fig. 6b (photoanodic in Fig. 6a). These observations are consistent with those for samples annealed without $Sr_3Ti_2O_7$ powder, indicating the $Sr_3Ti_2O_7$ reservoir also does not alter the intrinsic nature of the surface, but does alter the relative amounts of the two native terraces.

The observations made thus far indicate that increased temperature, time, or TiO_2 excess (in an adjacent powder reservoir) during high temperature anneals (>1000 °C) lead to an increased coverage of terraces that exhibit lower surface potentials and are reactive for the photo-oxidation of lead (*i.e.*, are photoanodic). Conversely, decreased temperature, time, or SrO excess lead to an increased coverage of terraces that appear as islands, exhibit higher surface potentials, and are reactive for the photo-reduction of silver (*i.e.*, are photocathodic). Assuming these trends could be extended to generate completely photoanodic or photocathodic surfaces, two $SrTiO_3(110)$ samples were annealed for 6 h at 1100 °C, one in the presence of a 2.0 g reservoir of TiO_2 and one in the presence of a 0.1 g reservoir of $Sr_3Ti_2O_7$ (this is a larger mass than used above). Topographic images of the surfaces before reaction are shown in Fig. 7a and b. Note that the sample heated in the presence of $Sr_3Ti_2O_7$ did not have the obvious terrace-step structure found in all other cases. For the sample annealed with TiO_2, 100% the surface was photoanodic, with all terraces being covered with lead-containing deposits (Fig. 7(c)), and 0% the terraces were photocathodic, with only the edges of the terraces having silver deposits (Fig. 7(e)). For the sample annealed with $Sr_3Ti_2O_7$, only 2% of the surface was photoanodic, or covered by the lead-containing deposits (Fig. 7(d)), while 98% was photocathodic, with the surface almost completely covered by reduced silver (Fig. 7(f)). Samples that were similarly annealed but without a reservoir (Fig. 4b) and with a smaller amount (0.02 g) of $Sr_3Ti_2O_7$ powder had 68% and 44% photoanodic surface area fractions, respectively.

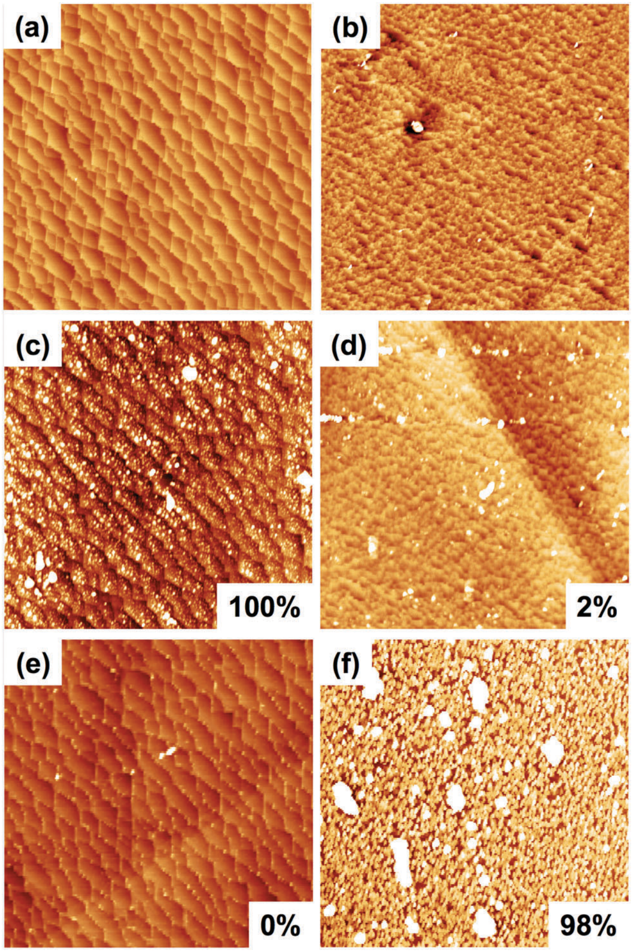

Fig. 7 Topographic AFM images of a sample annealed with 2 g TiO_2 powder: (a) the bare surface, (c) after lead photo-oxidation, and (e) after silver photo-reduction. Topographic AFM images of a sample annealed with 0.1 g $Sr_3Ti_2O_7$ powder: (b) the bare surface, (d) after lead photo-oxidation, and (f) after silver photo-reduction. Both samples were annealed at 1100 °C for 6 h. All images are 5 μm × 5 μm and the dark-to-light vertical scales are: (a and b) 0–2 nm, (c–e) 0–6 nm, and (f) 0–10 nm. The fractional coverage of photoanodic (c and d) and photocathodic (e and f) terraces are given in the lower right corners.

Discussion

The results show that the surface coverage of photoanodic and photocathodic terraces can be tuned through thermal annealing. The relative reactivity of all samples is summarized in Fig. 8, which plots the relative reactivity of all samples *versus* the annealing time, where temperature is denoted by the symbol

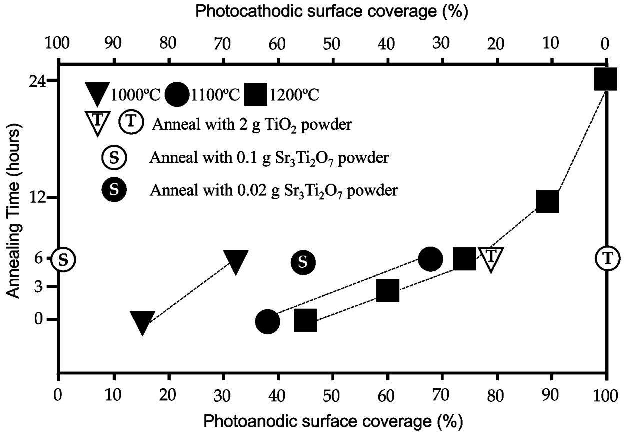

Fig. 8 The fractional coverage of photoanodic and photocathodic terraces *versus* the annealing time for samples shown in Fig. 2–7. As noted in the legend, all triangular, round, and square points represent samples heated at 1000, 1100, and 1200 °C, respectively. In cases where a TiO_2 or $Sr_3Ti_2O_7$ reservoir was used, the letters T or S, respectively, are placed within the symbols. The filled and unfilled circles designated with an S represent $Sr_3Ti_2O_7$ reservoirs of 0.02 and 0.1 g, respectively.

shape and the powder reservoir is indicated by letter within the symbol (see legend). The points connected by dashed lines were annealed at the same temperature (without a reservoir); if you follow these lines, it is apparent that shorter annealing times lead to more photocathodic surfaces. Comparing the location of the lines, it is clear that lower annealing temperatures lead to more photocathodic surfaces. Finally, focusing on the 6 h anneals, it is clear that the presence of TiO_2 makes the surface more photoanodic (at both 1000 and 1100 °C), while the presence of $Sr_3Ti_2O_7$ makes the surface more photocathodic (and the larger the mass of $Sr_3Ti_2O_7$ in the reservoir, the more photocathodic the surface, at 1100 °C).

The origin of these differences as a function of processing parameters is believed to arise from vapor phase transport of Sr. At elevated temperatures, the vapor pressure of SrO above $SrTiO_3$ is orders of magnitude higher ($P_{SrO} > 2$ Torr at 2000 °C)[43,44] than the vapor pressure of TiO_2 ($P_{TiO_x} \sim 10^{-10}$ Torr at 2000 °C).[45] Moreover, the presence of water vapor converts strontium oxide to a hydroxide, and $Sr(OH)_x$ has a vapor pressure which is larger by many orders of magnitude than that for SrO_x.[46] Assuming the concentration of SrO_x or $Sr(OH)_x$ in the initial atmosphere is below the equilibrium vapor pressure (approximating the local equilibrium as a closed system), then evaporation of Sr should occur from the $SrTiO_3$ crystal surface (in the absence of Sr-containing powders in the reservoir), leaving the surfaces Ti-rich. If the process is kinetically limited, longer and higher temperature annealing would increase the rate of Sr evaporation and surface evolution. Evaporation of surface species is consistent with the topographical observations made on the clean surfaces; the photocathodic terraces, which are those that decrease in fraction with increased time and temperature, are usually higher than the photoanodic terraces (see Fig. 2), suggesting that these areas are left behind as the terrace species evaporate. Based on this argument, the photoanodic and photocathodic terraces can be assigned as Ti-rich and Sr-rich, respectively. Although compositions of these terraces have not been measured in this work, the observations are similar to those made on $SrTiO_3(111)$ crystals.[21]

When $SrTiO_3(110)$ single crystals were annealed with Ti-rich and Sr-rich powders, the surfaces could be tuned toward the photocathodic and photoanodic extremes, respectively, even under the same temperature and time of anneals. This also can be explained through vapor phase Sr-species interactions between the crystal and the powder reservoirs. If the Sr-vapor reacts with the TiO_2 reservoir (which has a lower equilibrium vapor pressure), the condensation in the powder beds causes further Sr-evaporation from the crystal (to re-establish the equilibrium vapor pressure), leaving behind a more Ti-rich photoanodic $SrTiO_3(110)$ surface. This is in agreement with that observed on $SrTiO_3(111)$: an increased Ti-concentration at the surface of $SrTiO_3(111)$, as measured by XPS, was found for crystals annealed in the presence of TiO_2 excess reservoirs.[21] For the case of heating in the presence of $Sr_3Ti_2O_7$, similar arguments can be made. However, in this case, the Sr-rich phase also acts as a source of SrO_x, and one with a greater mass and much greater surface area than the single crystal. SrO_x can evaporate from the powder reservoir, transport to the single crystal, and either quickly establish equilibrium conditions, preventing or compensating for evaporation from the crystal, or re-condense on the crystal. For any one of the interactions, the surface is tuned to be a more Sr-rich photocathodic surface. It is important to establish a balance between the evaporation compensation mechanism and the condensation mechanism, as the relative Sr-composition was a function of the mass of $Sr_3Ti_2O_7$ in the reservoir, and new Sr-rich phases were found when too much $Sr_3Ti_2O_7$ was used.

Overall, our method of surface chemistry tuning achieves similar results to sputtering–annealing methods or etching–annealing methods,[35,47–49] though the precise structure of the surfaces may vary with annealing conditions. For example, either $(SrTiO)^{4+}$ or $(2O)^{4-}$ terminated $SrTiO_3(110)$ surfaces (which were all covered in Ti-rich oxide clusters) were prepared by tuning the Sr/Ti ratio at the surface using Ar^+ sputtering, followed with ultra-high vacuum annealing.[32] Our method of tuning the surface termination from nearly purely photocathodic to purely photoanodic by adding excess powders uses a similar concept, but the process can be carried out in air.

The result of these treatments is a $SrTiO_3(110)$ surface with two types of terraces with distinct surface potentials. The terraces that have the higher (more positive) surface potential promote reduction and are referred to photocathodic terraces. The terraces that have the lower (more negative) surface potential promote oxidation and are referred to as photoanodic terraces. This is similar to previously published observations on other surfaces, including polar terraces on $SrTiO_3(111)$,[21] polar domains on ferroelectric surfaces,[11] domains on ferroelastic surfaces,[13,14] thin films supported by ferroelectrics,[38,50,51] and different orientations of hematite.[18] All of these cases have the same correlation between surface potential and photochemical reactivity; the areas with a higher surface potential favor reduction reactions. This has been explained by presuming that the surface with the higher potential has reduced upward (or downward) band bending at surface. As a result, photogenerated electrons have a smaller energy barrier to get to the surface (or, in the case of downward band bending, are attracted to the surface) to participate in reduction reactions. On the other hand, areas with low surface potential have increased upward band bending. Upward band bending attracts holes to the surface for oxidation reactions and repels electrons. This qualitative interpretation has been supported quantitatively by simulations of the photochemical reactivity of thin TiO_2 films supported by ferroelectric $BaTiO_3$.[52,53]

As mentioned earlier, the $SrTiO_3(110)$ surface can be terminated by a (SrTiO) plane with a formal charge of +4 or by a (2O) plane with a formal charge of −4, and the spacing between these two planes of opposite charge is 1.38 Å (defined as N). However, the $SrTiO_3(110)$ surface is known to reconstruct. For example, a series of $(n \times 1)$ reconstructions has been observed after annealing in ultra-high vacuum.[54] For samples annealed at 1 atm in a 20% O_2 (balance N_2) between 900 °C and 1000 °C, (1×1) and (1×2) reconstructions made up of TiO_2 microfacets were found.[30] Other types of reconstructions have also been reported, depending on the annealing temperature, the time, and the environment.[27–31,34] In each of these cases, the surface can be thought of as a network of corner- or edge-sharing TiO_x units with varying stoichiometries that depend on how much Sr was lost during the annealing process. One aspect of these reconstructions that is important for the current work is that, independent of the reconstruction or the annealing environment, step heights measured between terraces of the same chemical composition are still even multiples of N.[35,37,55] Therefore, step height measurements can be used to determine if there is a change in the chemical composition of the terraces. In our experiment, it was determined that terraces separated by even-N heights have similar photochemical reactivity and surface potential while terraces separated by odd-N have different reactivity and surface potentials.

The potential difference between the two terraces originates from both surface charges and work function differences. It is assumed that the actual charges on the different terraces are reduced from the ideal +4 and −4 by reconstruction and adsorption. For example, for samples exposed to air and aqueous solutions, adsorption of hydroxyls is expected to alter the surface charge. For adsorption of water on $(1 \times n)$ reconstructed $SrTiO_3(110)$ surfaces, it was found that surfaces with highly oxidized Ti only weakly adsorb water,[33,34] while surfaces with reduced Ti and oxygen vacancies dissociate water molecules at the oxygen vacancies, resulting in strongly adsorbed hydroxyl groups. Differences in the work functions of the ideal $(SrTiO)^{4+}$ and $(2O)^{4-}$ terminations have been computed, with the $(2O)^{4-}$ surface having a work function that is 1 eV lower than the $(SrTiO)^{4+}$ surface.[56] Based on these previous observations, differences in charge, adsorbed species, and work functions probably all contribute to the difference in the measured potential and reactivity of the two different terraces observed on $SrTiO_3(110)$ (and (111)[21]), and it is difficult to assign a relative importance to each factor.

The main difference between the current paper and our earlier study of $SrTiO_3(111)$[21] is that the surface coverage of photoanodic and photocathodic terraces of $SrTiO_3(110)$ have been tuned over a much wider range than $SrTiO_3(111)$. By varying temperature and time, or adding reservoirs of Ti-rich or Sr-rich powders, the surface can be continuously changed from purely photoanodic to photocathodic. Therefore, it is possible to optimize the overall photochemical reactivity for the reaction of interest. For example, if the catalyst is designed to degrade organic compounds, a high percentage of photoanodic terraces might be the most efficient. For water splitting, the relative areas of the terraces should be adjusted so that reduction and oxidation half reactions occur at the same rate. On an n-type semiconductor such as $SrTiO_3$, this is likely to be a surface that favors the minority carrier (oxidation) reaction.

Conclusions

$SrTiO_3(110)$ surfaces annealed in air at temperatures between 1000 °C and 1200 °C exhibit two types of terraces with distinct surface potentials. The different types of terraces are separated by odd integer multiples of the interplanar spacing, corresponding to different chemical terminations of the bulk crystal. The terraces with the more positive (less positive) surface potential promote photo-reduction (photo-oxidation) reactions as more electrons (holes) are attracted to surface. Therefore, the more positive terraces are photocathodic and the less positive terraces are photoanodic. The relative surface coverage of these two terraces, and the surface reactivity, can be controlled by the temperature, duration, and chemical composition of the adjacent powder during annealing. Samples annealed at higher temperatures and for longer times have a higher fraction of photoanodic surface area. Annealing with TiO_2 powder promotes photoanodic surfaces while annealing with $Sr_3Ti_2O_7$ powder promotes photocathodic surfaces. By annealing with a $Sr_3Ti_2O_7$ reservoir, it was possible to create a surface that was 98% photocathodic. These annealing treatments make it possible to adjust the $SrTiO_3(110)$ surface from essentially completely photocathodic to completely photoanodic, or to any ratio appropriate for a specific photochemical reaction.

Acknowledgements

The authors acknowledge the support of National Science Foundation grant DMR 1609369. The authors acknowledge use of the Materials Characterization Facility at Carnegie Mellon University supported by grant MCF-677785.

Notes and references

1 T. Hisatomi, J. Kubota and K. Domen, *Chem. Soc. Rev.*, 2014, **43**, 7520–7535.

2 S. J. A. Moniz, S. A. Shevlin, D. J. Martin, Z.-X. Guo and J. Tang, *Energy Environ. Sci.*, 2015, **8**, 731–759.

3 F. E. Osterloh, *Chem. Soc. Rev.*, 2013, **42**, 2294–2320.

4 Y. Tachibana, L. Vayssieres and J. R. Durrant, *Nat. Photonics*, 2012, **6**, 511–518.

5 K. Maeda and K. Domen, *J. Phys. Chem. Lett.*, 2010, **1**, 2655–2661.

6 Y. Qu and X. Duan, *Chem. Soc. Rev.*, 2013, **42**, 2568–2580.

7 L. Li, P. A. Salvador and G. S. Rohrer, *Nanoscale*, 2014, **6**, 24–42.

8 D. Tiwari and S. Dunn, *J. Mater. Sci.*, 2009, **44**, 5063–5079.

9 S. Sato and J. M. White, *Chem. Phys. Lett.*, 1980, **72**, 83–86.

10 S. Dunn, P. M. Jones and D. E. Gallardo, *J. Am. Chem. Soc.*, 2007, **129**, 8724–8728.

11 J. L. Giocondi and G. S. Rohrer, *J. Phys. Chem. B*, 2001, **105**, 8275–8277.

12 Y. Inoue, K. Sato and H. Miyama, *J. Phys. Chem.*, 1986, **90**, 2809–2810.

13 R. Munprom, P. A. Salvador and G. S. Rohrer, *Chem. Mater.*, 2014, **26**, 2774–2776.

14 R. Munprom, P. A. Salvador and G. S. Rohrer, *J. Mater. Chem. A*, 2016, **4**, 2951–2959.

15 X. Wang, Q. Xu, M. Li, S. Shen, X. Wang, Y. Wang, Z. Feng, J. Shi, H. Han and C. Li, *Angew. Chem., Int. Ed. Engl.*, 2012, **51**, 13089–13092.

16 D. Yang, H. Liu, Z. Zheng, Y. Yuan, J.-C. Zhao, E. R. Waclawik, X. Ke and H. Zhu, *J. Am. Chem. Soc.*, 2009, **131**, 17885–17893.

17 R. Li, F. Zhang, D. Wang, J. Yang, M. Li, J. Zhu, X. Zhou, H. Han and C. Li, *Nat. Commun.*, 2013, **4**, 1432.

18 Y. Zhu, A. M. Schultz, G. S. Rohrer and P. A. Salvador, *J. Am. Ceram. Soc.*, 2016, **99**, 2428–2435.

19 J. L. Giocondi and G. S. Rohrer, *J. Am. Ceram. Soc.*, 2003, **86**, 1182–1189.

20 B. Liu, L. Ma, L.-C. Ning, C.-J. Zhang, G.-P. Han, C.-J. Pei, H. Zhao, S.-Z. Liu and H.-Q. Yang, *ACS Appl. Mater. Interfaces*, 2015, **7**, 6109–6117.

21 Y. Zhu, P. A. Salvador and G. S. Rohrer, *Chem. Mater.*, 2016, **28**, 5155–5162.

22 G. Liu, J. C. Yu, G. Q. Lu and H.-M. Cheng, *Chem. Commun.*, 2011, **47**, 6763–6783.

23 D. Wang, H. Jiang, X. Zong, Q. Xu, Y. Ma, G. Li and C. Li, *Chem. – Eur. J.*, 2011, **17**, 1275–1282.

24 A. Navrotsky and D. J. Weidner, *Geophysical Union Geophysical Monograph Series*, 1989, vol. 45, p. 119.

25 J. G. Mavroides, J. A. Kafalas and D. F. Kolesar, *Appl. Phys. Lett.*, 1976, **28**, 241–243.

26 K. van Benthem, C. Elsasser and R. H. French, *J. Appl. Phys.*, 2001, **90**, 6156–6164.

27 H. Bando, Y. Aiura, Y. Haruyama, T. Shimizu and Y. Nishihara, *J. Vac. Sci. Technol., B: Microelectron. Nanometer Struct.–Process., Meas., Phenom.*, 1995, **13**, 1150–1154.

28 J. Brunen and J. Zegenhagen, *Surf. Sci.*, 1997, **389**, 349–365.

29 N. Erdman and L. D. Marks, *Surf. Sci.*, 2003, **526**, 107–114.

30 A. Gunhold, K. Gomann, L. Beuermann, V. Kempter, G. Borchardt and W. Maus-Friedrichs, *Surf. Sci.*, 2004, **566**, 105–110.

31 D. M. Kienzle, PhD thesis, Northwestern University, 2013.

32 Z. Wang, F. Yang, Z. Zhang, Y. Tang, J. Feng, K. Wu, Q. Guo and J. Guo, *Phys. Rev. B: Condens. Matter Mater. Phys.*, 2011, **83**, 155453.

33 W. T. Li, S. M. Liu, S. Wang, Q. L. Guo and J. D. Guo, *J. Phys. Chem. C*, 2014, **118**, 2469–2474.

34 Z. M. Wang, X. F. Hao, S. Gerhold, Z. Novotny, C. Franchini, E. McDermott, K. Schulte, M. Schmid and U. Diebold, *J. Phys. Chem. C*, 2013, **117**, 26060–26069.

35 A. Biswas, P. B. Rossen, C. H. Yang, W. Siemons, M. H. Jung, I. K. Yang, R. Ramesh and Y. H. Jeong, *Appl. Phys. Lett.*, 2011, **98**, 051904.

36 F. Sanchez, C. Ocal and J. Fontcuberta, *Chem. Soc. Rev.*, 2014, **43**, 2272–2285.

37 Y. Mukunoki, N. Nakagawa, T. Susaki and H. Y. Hwang, *Appl. Phys. Lett.*, 2005, **86**, 171908.

38 N. V. Burbure, P. A. Salvador and G. S. Rohrer, *Chem. Mater.*, 2010, **22**, 5831–5837.

39 J. L. Giocondi and G. S. Rohrer, *Top. Catal.*, 2008, **49**, 18–23.

40 K. Tanaka, K. Harada and S. Murata, *Sol. Energy*, 1986, **36**, 159–161.

41 J. Torres and S. Cerveramarch, *Chem. Eng. Sci.*, 1992, **47**, 3857–3862.

42 D. Necas and P. Klapetek, *Cent. Eur. J. Phys.*, 2012, **10**, 181–188.

43 C. Guguschev, D. Klimm, F. Langhans, Z. Galazka, D. Kok, U. Juda and R. Uecker, *CrystEngComm*, 2014, **16**, 1735–1740.

44 R. H. Lamoreaux, D. L. Hildenbrand and L. Brewer, *J. Phys. Chem. Ref. Data*, 1987, **16**, 419–443.

45 P. M. Martin, *Handbook of deposition technologies for films and coatings: science, applications and technology*, William Andrew, 2009.

46 T. Zhang and S. Wang, in *Nanostructured and Advanced Materials for Fuel Cells*, ed. S. P. Jiang and P. K. Shen, CRC Press, Taylor Francis Group, Boca Raton, FL, 2008, p. 58.

47 J. Chang, Y.-S. Park and S.-K. Kim, *Appl. Phys. Lett.*, 2008, **92**, 152910.

48 T. D. Doan, J. L. Giocondi, G. S. Rohrer and P. A. Salvador, *J. Cryst. Growth*, 2001, **225**, 178–182.

49 W. M. Sigmund, M. Rotov, Q. D. Jiang, J. Brunen, J. Zegenhagen and F. Aldinger, *Appl. Phys. A: Mater. Sci. Process.*, 1997, **64**, 219–220.

50 N. V. Burbure, P. A. Salvador and G. S. Rohrer, *Chem. Mater.*, 2010, **22**, 5823–5830.

51 Y. L. Zhang, A. M. Schultz, P. A. Salvador and G. S. Rohrer, *J. Mater. Chem.*, 2011, **21**, 4168–4174.

52 J. J. Glickstein, P. A. Salvador and G. S. Rohrer, *J. Phys. Chem. C*, 2016, **120**, 12673–12684.

53 J. J. Glickstein, P. A. Salvador and G. S. Rohrer, *J. Mater. Chem. A*, 2016, **4**, 16085–16093.

54 B. C. Russell and M. R. Castell, *Phys. Rev. B: Condens. Matter Mater. Phys.*, 2008, **77**, 245414.

55 R. Bachelet, F. Valle, I. C. Infante, F. Sanchez and J. Fontcuberta, *Appl. Phys. Lett.*, 2007, **91**, 251908.

56 A. Pojani, F. Finocchi and C. Noguera, *Surf. Sci.*, 1999, **442**, 179–198.

Electronic Supplementary Material (ESI) for Physical Chemistry Chemical Physics.

Supplemental Information for:

Controlling the termination and photochemical reactivity of the $SrTiO_3$ (110) surface

Yisi Zhu, Paul A. Salvador, and Gregory S. Rohrer*

Carnegie Mellon University, Department of Materials Science and Engineering, Pittsburgh, PA 15213

0. Overview

This document contains the supplemental information supporting the main text of the manuscript. Specifically, AFM images are given for samples annealed in air at 1200 °C for different lengths of time, after photo-reduction (S1) and before any photo-reaction (S2). These images are related to the images given in Figure 3 of the main text, showing photo-oxidation of the same surfaces. Also, AFM images are given for samples annealed in air at 1100 and 1000 °C, for both 0 and 6 h each, after photo-reduction (S2) and before any photo-reaction (S4). These images are related to the images given in Figure 4 of the main text showing photo-oxidation of the same surfaces. None of these samples were annealed with powder reservoirs. The images support the complementary nature of the photo-reactive surfaces and the different reactive nature of the two sets of terraces on the surface.

1. Silver photo-reduction for samples annealed at 1200 ºC

Fig. S1 shows topographic AFM images after silver photo-reduction of four samples annealed for different amounts of time at 1200 ºC in air, without powder reservoirs. The surfaces were imaged at the same locations as in Fig. 3 of the main text. The bright contrast in the images corresponds to silver deposits. The fractional coverages of silver (i.e., the photocathodic area fractions) are 53 , 40, 11, and 2 % for the samples annealed for 0, 3, 12, and 24 h, respectively. When compared to Fig. 3, the surface reactivity is complementary: photo-reduction and photo-oxidation reactions happen on different terraces. Thus, while the photoanodic area fraction increases with annealing time, the photocathodic area fraction decreases with increasing annealing time.

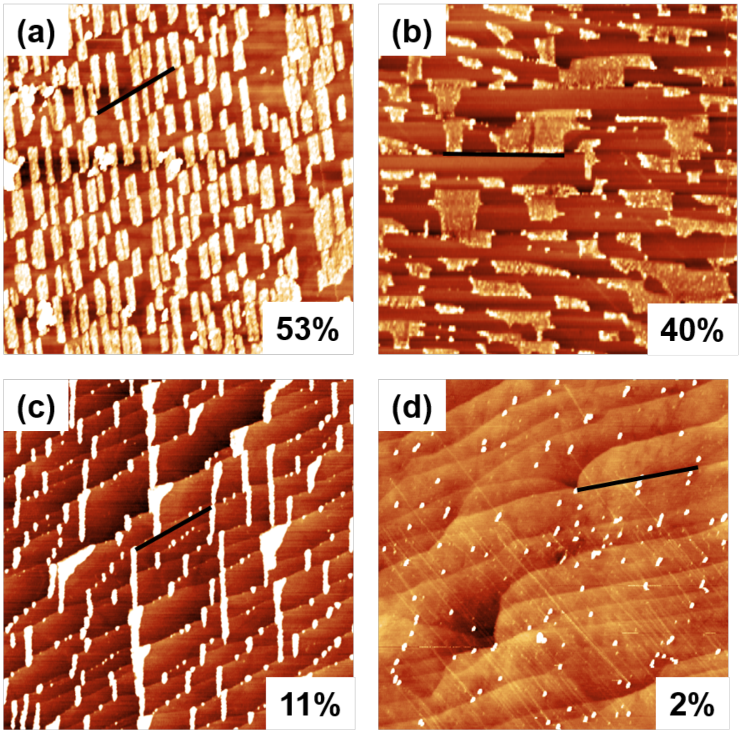

Figure S1. Surface topography AFM images of the photo-reduced silver distribution on samples annealed at 1200 °C for (a) 0 hour (b) 3 hours (c) 12 hours and (d) 24 hours. All images are 5 µm × 5 µm laterally and the dark-to-light vertical scales are 0 – 4 nm. The percentage in lower corner marks the fractional coverage of photocathodic terraces in each image. The black lines mark the same locations that are marked in Fig. 3 and Fig. S2.

2. Surface topography for samples annealed at 1200 ºC

Fig. S2 shows topographic AFM images of the clean, annealed surfaces of the same samples and in the same as the images of Fig. 3 and Fig. S1. The two sets of terraces (described in the main text for Fig. 2) are evident in Fig. S2(a) and (b). Again, the set of terraces with bright contrast in topography are reactive for photo-reduction (are photocathodic). The topographic contrast is not as obvious in Fig. S2(c) and (d). In S2(c), the edges of terraces where the step edge changes direction is often brighter, and this does correspond to the reactivity in Fig. S1(c). But the relative area is only 11 % photocathodic, and thus these terraces are smaller and narrower, and less obvious. There is only one set of terraces in S2(d), and therefore no contrast; this surface is 100 % photoanodic (Fig. 3). The small (2 %) photocathodic activity observed in S1(d) is not correlated with any terrace feature.

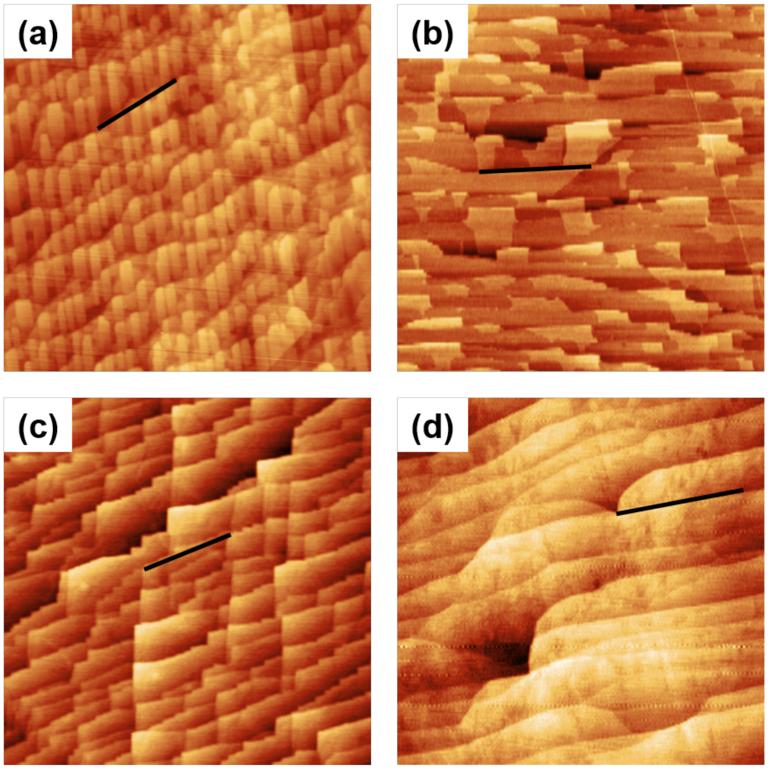

Figure S2. Surface topography AFM image of clean surfaces of samples annealed at 1200 °C for (a) 0 hour (b) 3 hours (c) 12 hours and (d) 24 hours. All images are 5 μm × 5 μm laterally and the dark-to-light vertical scales are 0 – 2 nm. The black lines mark the same locations that are marked in Fig. 3 and Fig. S1.

3. Silver photo-reduction for samples annealed at 1100 ºC and 1000 ºC

Figures S3(a) and (b) (Figures S3(c) and (d)) show topographic images of samples heated to 1100 °C (1000 °C) for 0 h and 6 h, respectively, after the photo-reduction of silver. Images show the same locations as in the images in Fig. 4 of the main text. The bright contrast corresponds to the silver deposits. The sample shown in Fig. S3(c) has the smallest terraces and, because the size of the silver particles produced after reaction are significant in comparison to the terrace width, the terrace contrast becomes grainy. The fractional coverage of photocathodic terraces decreases with annealing time, from 60 to 32 % (80 to 65 %) for 0 h and 6 h anneals at 1100 °C (1000 °C). When compared to Fig. 4, the surface reactivity is complementary: photo-reduction and photo-oxidation reactions happen on different terraces and the photocathodic area fraction decreases with the annealing time (and temperature).

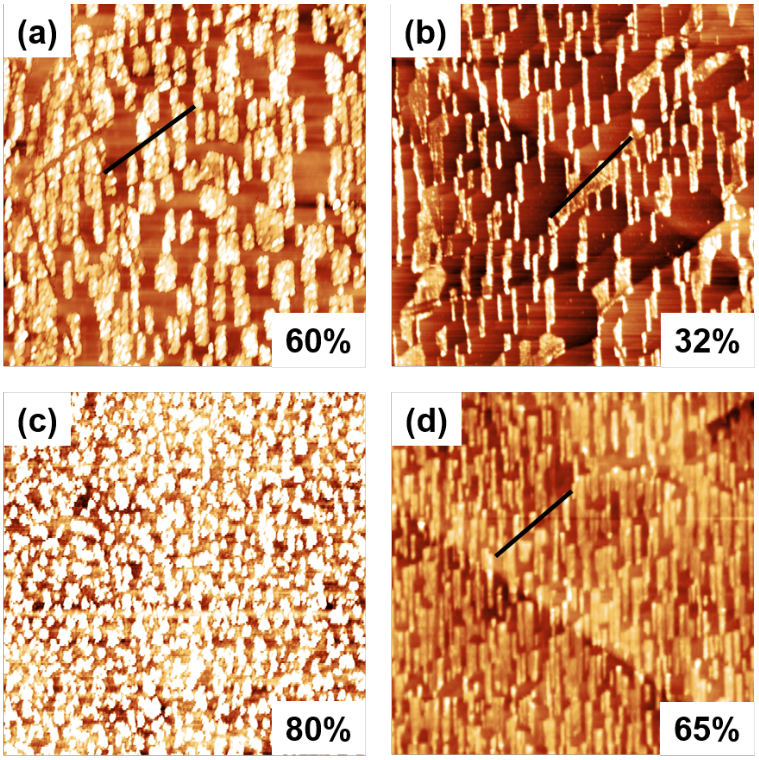

Figure S3. Surface topography AFM images after silver photo-reduction for samples annealed at 1100 °C for (a) 0 hour (b) 6 hours and samples annealed at 1000 °C for (c) 0 hour (d) 6 hours. (a), (b), and (d) are 5 μm × 5 μm and (c) is 3 μm × 3 μm laterally. The dark-to-light vertical scales are 0 – 4 nm. The black lines mark the same locations that are marked in Fig. 4 and Fig. S4.

4. Surface topography for samples annealed at 1100 ºC and 1000 ºC

Fig. S4 shows topographic AFM images of the clean annealed surfaces of the same samples and at the same locations as in Fig. 4 and Fig. S3. The two sets of terraces (described in the main text for Fig. 2) are evident for all samples in Fig. S4. One set of terraces exhibits a range of bright contrast, and these terraces sit upon another set of terraces that exhibit a darker range of contrast. The scratches (straight dark lines) in Fig. S4(d) were inadvertently introduced during handling, and thus was not present when the images in Fig. 4(d) and Fig. S3(d) were recorded. Comparing Fig. S4, S3, and 4, it is clear that the bright set of terraces in topography are reactive for photo-reduction (are photocathodic), while the darker set of terraces in topography are reactive for photo-oxidation (are photoanodic). This correlation is less clear for the sample shown in Fig. (c) (for each figure), because its terraces are narrow and the distribution of reaction products make the image appear grainy.

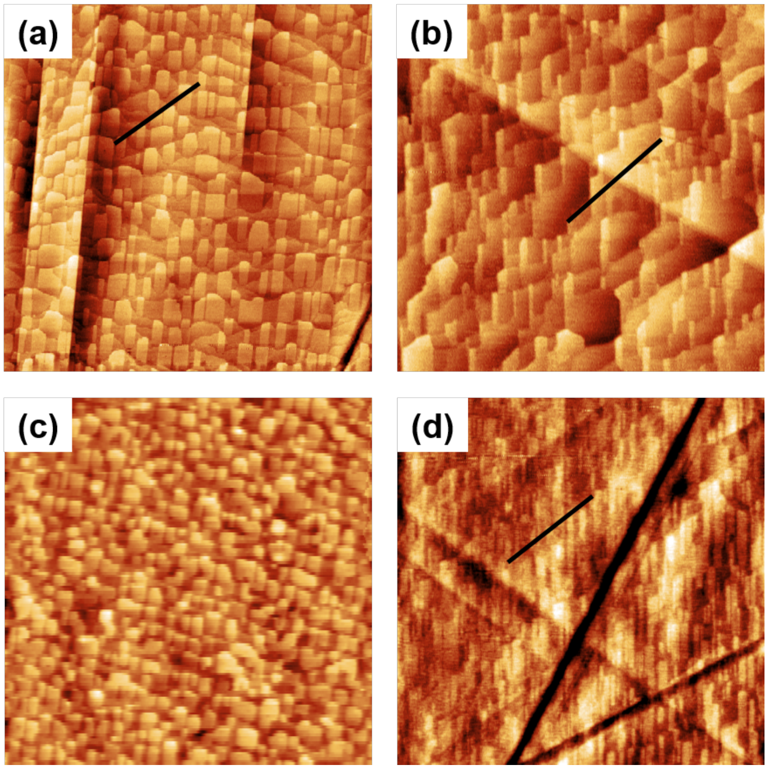

Figure S4. Surface topography AFM images of clean surfaces of samples annealed at 1100 °C for (a) 0 hours and (b) 6 hours and samples annealed at 1000 °C for (c) 0 hours and (d) 6 hours. The dimensions of the images are: (a), (b), and (d) 5 μm × 5 μm and (c) 3 μm × 3 μm laterally. The dark-to-light vertical scales are 0 – 2 nm. The black lines mark the same locations that are marked in Fig. 4 and Fig. S3.